Check for updates

Plasmonic Cu-supported amorphous RuP for efficient photothermal CO2 hydrogenation to CO†

Xiuping Li,‡[b] Jiaqi Wang,‡[a] Bolin Yin,[b] Kaihong Liu,[b] Jingjing Zhao,[b] Bo Jiang[b] and Hexing Li [ID] *[ab]

The hydrogenation of carbon dioxide into profitable chemicals is a viable path toward achieving the objective of carbon neutrality. However, the typical approach for hydrogenation of CO_2 heavily relies on thermally driven catalysis at high temperatures, which is not aligned with the goals of carbon neutrality. Thus, there is a critical need to explore new catalytic methods for the high-efficiency conversion of CO_2. Herein, we present a new class of catalysts, featuring phosphorus-doped amorphous ruthenium nanoparticles supported on copper nanoparticles, which capitalizes on the plasmonic effects of copper to achieve the photothermal transformation of CO_2 to CO within a gas−solid flow system. Our findings indicated that the reaction efficiency in the presence of photothermal energy was over eight times greater than that with thermal energy alone. The catalyst system exhibited nearly 100% selectivity towards CO under mild conditions, with an impressive CO yield of 123.16 mmol g^{-1} h^{-1}. This study highlights the significant potential of amorphous metal phosphides in photocatalytic CO_2 hydrogenation under mild conditions and offers a fresh avenue for the robust catalysis of amorphous materials.

1. Introduction

Transforming carbon dioxide into profitable chemicals through green hydrogenation represents a favourable strategy for addressing energy-related crises and environmental degradation.[1–4] This transformation is particularly beneficial as it repurposes CO_2 into basic chemicals for renewable compounds without relying on traditional fossil fuel sources.[5–7] The hydrogenation process of CO_2 commonly results in the formation of C1 chemicals, such as carbon monoxide (CO), methane (CH_4), and methanol (CH_3OH).[8–12] CO is particularly valuable as it can be integrated into existing synthetic pathways to produce a range of useful chemicals, including alcohols, liquid hydrocarbons, and organic acids.[13–16] However, the hydrogenation of CO_2 for selectively producing CO, known as the reverse water–gas shift reaction (RWGS), is complex.[17–19] This is due to the competing reactions for formation of undesired side products, such as methanol and methane.

$$CO_2 + H_2 \leftrightarrow CO + H_2O \qquad (1)$$

[a]School of Chemistry and Molecular Engineering, East China University of Science and Technology, 130 Meilong Road, Shanghai 200237, China

[b]The Education Ministry Key Lab of Resource Chemistry, Shanghai Key Laboratory of Rare Earth Functional Materials, Shanghai Normal University, Shanghai 200234, China. E-mail: hexing-li@shnu.edu.cn

† Electronic supplementary information (ESI) available. See DOI: https://doi.org/10.1039/d4ra07361d

‡ Xiuping Li and Jiaqi Wang are contributed equally to this work.

The transformation of CO_2 into useful chemicals through hydrogenation is constrained owing to the thermodynamic stability of CO_2 molecules.[20–23] As a result, catalytic processes for the hydrogenation of CO_2 generally necessitate energy-intensive input (*i.e.*, high temperatures and pressures). To reduce the substantial energy expenditure, there is a critical demand for the development of catalysts that can facilitate reactions with minimal energy input. This obstacle could be surmounted by employing advanced photocatalytic systems that are capable of initiating reactions under mild conditions, thereby decreasing the reliance on conventional thermal activation pathways that are driven by energy-intensive phonon mechanisms.[24,25]

In the recent past, the realm of plasmonics has captured the attention of the scientific community owing to its remarkable ability to absorb light across the entire spectrum and potent photothermal conversion capabilities.[26] Metal nanoparticles that are active in plasmonics, including gold, silver, copper, and aluminum, have been recognized for their photocatalytic roles in a broad spectrum of chemical transformations.[26–29] These plasmonic metals possess the property of localized surface plasmon resonance (LSPR), which amplifies the light absorption capacity of a photocatalyst. By leveraging LSPR, these metals become excitable under illumination, resulting in a substantial enhancement of the local electric field. A high concentration of hot electrons is also generated on the surface of the plasma structure.[30–32] Consequently, this enhancement leads to milder reaction conditions and a reduction in side reactions, thereby increasing the selectivity towards target products. Copper nanostructures are especially noteworthy due

to their cost-effectiveness and pronounced LSPR effects across a wide range of wavelengths from UV to NIR.[26] New findings indicate that hybrid structures, integrating plasmonic metal nanoparticles with materials that possess inherent catalytic activity, can significantly boost the efficiency and selectivity of photocatalytic reactions.

The fusion of phosphorus with transition metal compounds presents promising prospects for catalyzing hydrogen and oxygen evolution reactions and CO_2 hydrogenation.[33–35] For example, Chen et al., introduced a novel anionic substitution technique to significantly improve the RuP catalytic efficiency for HER.[34] The resultant N–RuP/NPC catalyst exhibited exceptional performance, surpassing the activity of many platinum-free alternatives with record-breaking turnover frequencies. Furthermore, the incorporation of phosphorus through doping can significantly modulate the electronic configuration of Ru, thereby creating a plethora of active sites that facilitate CO_2 adsorption.[36] Therefore, ruthenium phosphide (RuP) is considered as an exceptional candidate for the hydrogenation of carbon dioxide.

In this study, we utilized a straightforward chemical reduction approach to fabricate a catalyst comprising amorphous ruthenium nanoparticles doped with phosphorus and supported on copper nanoparticles. The catalyst was subsequently applied to the photothermal catalysis of CO_2 under hydrogenation conditions. The catalyst exhibits enhanced selectivity and stability for the photothermal hydrogenation of CO_2 through the manipulation of Ru electronic configurations. The catalytic activity of 123.16 mmol g^{-1} h^{-1} was attained at a temperature of 300 °C under atmospheric pressure. The findings from our experiments indicate that the integration of copper nanoparticles effectively channelled light energy into the catalytic framework, resulting in a nearly eightfold increase in catalytic activity in the presence of photothermal effects compared to thermally-driven processes alone. This work offers valuable perspectives on the development of copper-based plasmonic catalysts.

2. Experimental section

2.1 Materials and reagents

In this study, all chemicals were procured from Aladdin Reagent Company. Unless otherwise specified, the reagents used throughout our experiments were of analytical grade and did not require additional purification.

2.2 Catalyst preparation

Taking the synthesis of the 4% RuP/Cu catalyst as an example, 0.8 g of $CuCl_2 \cdot 2H_2O$ powder was introduced into a beaker containing 100 mL of ultrapure water under vigorous stirring. Subsequently, 3.45 mL of a $RuCl_3$ solution (10 mg mL^{-1}) was added to the above solution, followed by the addition of 1.6 g sodium hypophosphite and 0.28 g sodium citrate. Then, the pH of the mixed solution was stabilized at about 11.75 with 2 M NaOH solution. Thereafter, the solution was kept at 90 °C in an oil bath for 8 hours at a stirring speed set to 600 rpm. Once the

oil bath treatment was complete, the precipitate was washed 6 times with a mixture of water and ethanol and then dried overnight in an oven at 80 °C to obtain the catalyst precursor 4% RuP/CuO. After the precursor was thoroughly dried, a measured amount of the precursor powder was weighed using a quartz boat and placed in a tubular furnace. Finally, the precursor was kept at 300 °C for two hours in a 10% H_2/Ar atmosphere with a temperature gradient of 5 °C min^{-1} to obtain the final catalyst, 4% RuP/Cu.

The preparation of Cu serves as a control to isolate variables. It was prepared in much the same way as 4% RuP/Cu, with the exception of the omission of the $RuCl_3$ solution.

2.3 Catalyst characterization

The nitrogen adsorption–desorption isotherms were acquired at 77 K utilizing a Micromeritics ASAP 2010 analyzer, employing the Brunauer–Emmett–Teller (BET) and Barrett–Joyner–Halenda (BJH) methods to determine the specific surface area and pore volume, respectively. The wide-angle X-ray diffraction (XRD) analysis was conducted on a Rigaku Ultimate IV instrument utilizing CuKα radiation ($\lambda = 1.54$ Å) at a voltage and current of 40 kV and 40 mA, respectively. X-ray photoelectron spectroscopy (XPS) measurements were executed with a Thermo Scientific K-Alpha system, with the C 1s peak set at 284.8 eV for charge referencing. Transmission electron microscopy (TEM) and scanning transmission electron microscopy (STEM) were conducted using a JEOL JEM 2100F electron microscope operating at 200 kV. The temperature-programmed desorption (TPD) analysis of the catalysts was performed using a Micromeritics AutoChem II analyzer with a thermal conductivity detector (TCD) in a 10% H_2/Ar atmosphere. Samples were pretreated at 300 °C under an Ar flow for 30 minutes, followed by H_2 adsorption at ambient temperature for 30 minutes. After an Ar purge for 30 minutes, the TPD procedure was initiated with a heating rate of 10 °C per minute.

2.4 Activity measurement

The catalytic activity for CO_2 hydrogenation was evaluated in a self-made flow reactor system (Fig. S1†). The products were analyzed online using a gas chromatography (GC) system (Agilent, GC7890B) equipped with both a thermal conductivity detector (TCD) and a flame ionization detector (FID). Typically, the catalyst was homogeneously mixed with 0.5 g of quartz sand, which was then packed into the central window of a homemade quartz tube (10 mm × 10 mm × 2 mm) and secured with quartz wool to prevent dispersion. A 300 W xenon lamp (Beijing Poffet) served as the light source, and a circulating water-cooling system was installed at the sapphire window of the reactor to eliminate the photothermal effects induced by the xenon lamp. In a typical test, the catalyst was placed in a raw gas environment at room temperature, with the flow of the raw gas controlled by a mass flowmeter. After flushing with the raw gas for 30 minutes, the reactor temperature was raised to the target reaction temperature. Also, the real-time monitoring of the reaction temperature was conducted using two thermocouples. In the photothermal reaction, the

thermal effect was entirely provided by external heating. All feed gases contained 25% argon as an internal standard. After stabilization for 60 minutes, the light source was turned on to initiate the photothermal reaction. The output gases were analyzed in real-time using GC. Quantitative analysis of the gaseous products was performed using both the FID and TCD detectors.

3. Results and discussion

3.1 Synthesis and characterization of catalysts

The morphology and structure of the typical samples were first characterized using TEM. As shown in Fig. 1, the Cu nanoparticles in 4% RuP/Cu were primarily in the size range of 1.1 ± 0.4 nm (Fig. 1a and inset of Fig. 1a). Fig. 1b indicates clear lattice fringes of 0.178 nm and 0.210 nm corresponding to the Cu(200) plane and Cu(111) plane, respectively. No crystal fringes were observed at the edges of the nanoparticles, indicating that RuP was predominantly amorphous in the structure. The energy-dispersive X-ray spectroscopy (EDS) results reveal the uniform dispersion of Cu, Ru, and P elements within the 4% RuP/Cu catalyst (Fig. 1c–f).

The phase structure of the prepared samples was determined using XRD. As depicted in Fig. 2a, the diffraction peaks for the Cu nanoparticle catalysts with varying RuP loadings appear at approximately 43°, 46°, and 74°, which coincide with those of Cu.[37] A significant peak observed prior to 40° corresponds to the characteristic peak of Cu_2O, which may arise from oxidation during catalyst storage. The XRD patterns of the catalysts with different RuP loadings reveal a rightward shift in the full-width peak positions upon the introduction of RuP, which is attributable to changes in the lattice parameters. The lattice parameter of Cu is 361.49 pm, whereas that of Ru is 270.59 pm; the introduction of an element with a smaller lattice parameter component results in the rightward shift of the peaks.[38,39] The absence of Ru diffraction peaks may be due to the amorphous structure of RuP and the high crystallinity of the Cu nanoparticles.

Subsequently, the electronic states of Cu, Ru, and P in 4% RuP/Cu were investigated using XPS. In the XPS spectrum of 4% RuP/Cu (Fig. 2b), the Cu peaks were fitted using Lorentz–Gaussian functions, with two fitted peaks corresponding to Cu(0) for Cu^0 $2p_{3/2}$ and Cu^0 $2p_{1/2}$ positioned at 932.4 eV and 952.3 eV, respectively.[37] The peaks for Cu(II) correspond to Cu^{2+} $2p_{3/2}$ and Cu^{2+} $2p_{1/2}$, located at 933.5 eV and 953.6 eV, respectively.[37] The Cu LMM auger electron spectra of 4% RuP/Cu (Fig. S2†) exhibited a peak at 568.1 eV, suggesting the existence of Cu^0 species in 4% RuP/Cu. The predominance of zerovalent Cu in 4% RuP/Cu, as indicated by the relative areas of their fitted peaks, was consistent with the findings from XRD. Fig. 2c displays the main peak for P 2p at 133 eV, characteristic of phosphorus bonded with oxygen in phosphate species, while the peaks corresponding to the $sp_{1/2}$ and $sp_{3/2}$ hybridization of P with Ru appear at 130.3 eV and 128.6 eV, respectively. Fig. 2d reflects the two hybridized peaks of Ru 3p orbitals that correspond to the P 2p orbitals, appearing at 484.9 eV and 462.6 eV, respectively.[33,34,40]

The specific surface area of the prepared samples was measured through N_2 adsorption–desorption isotherms (Fig. 3a and Table S1†), revealing the high specific surface area of Cu nanoparticles and the low specific surface area of RuP. The large specific surface area of Cu nanoparticles is likely due to their small particle size. After loading RuP, the specific surface area of the 4% RuP/Cu sample decreased, which is attributed to the wrapping of Cu nanoparticles by RuP, leading to an increase in the particle size.

To further investigate the interaction between RuP and Cu, we characterized the samples using H_2-TPD (Fig. 3b). All catalysts in the figure exhibit three desorption peaks corresponding to three different adsorption modes: a hydrogen adsorption peak for metallic Cu around the low-temperature region of 90 °C, a hydrogen adsorption peak for Cu interacting with P elements around the medium-temperature region of 140 °C, and a hydrogen adsorption peak for Cu interacting with O elements in the high-temperature region of 260 °C. Comparing the blue and red lines in the figure, it can be observed that the addition of RuP caused a leftward shift in the adsorption peak
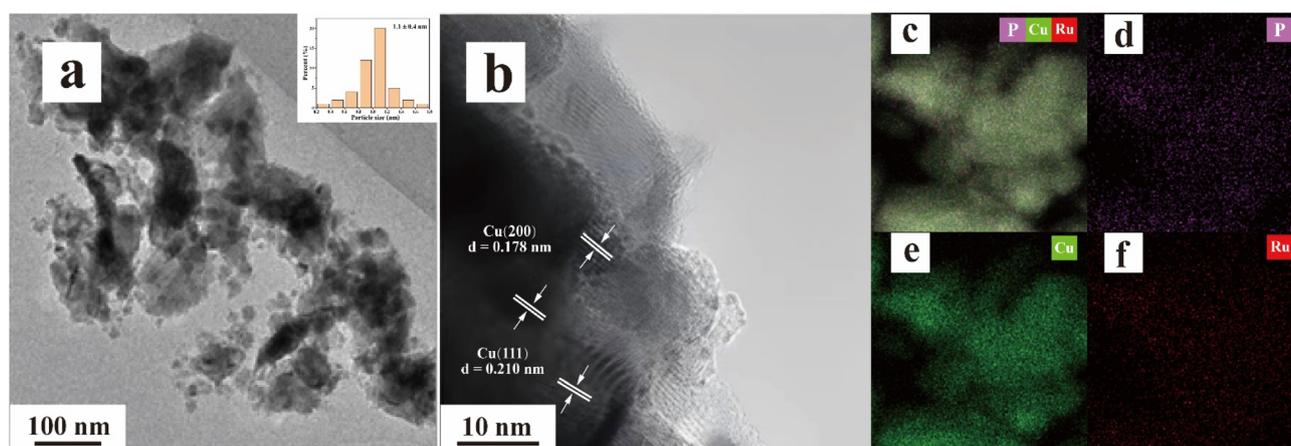

Fig. 1 (a) and (b) TEM images and particle size distribution (inset a) as well as (c)–(f) element mappings of 4% RuP/Cu.
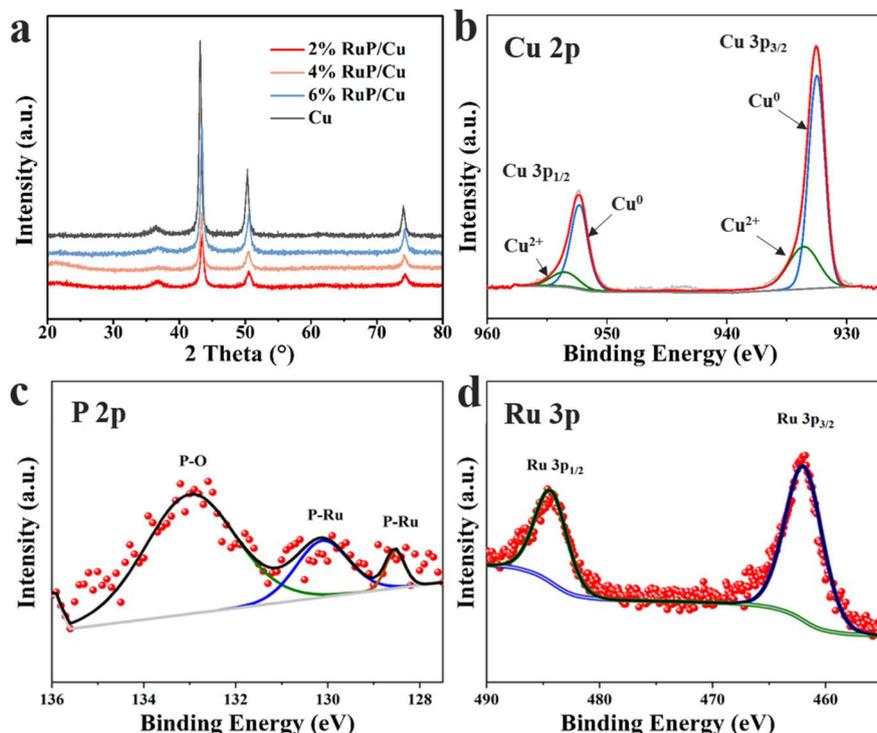
Fig. 2 (a) XRD patterns of different catalysts; XPS spectra of the (b) Cu 2p, (c) P 2p and (d) Ru 3p levels of 4% RuP/Cu.

near 140 °C in the medium-temperature region. This is because Ru has a higher electronegativity than Cu, and the electron-deficient Ru further facilitates the flow of electrons from Cu to Ru, increasing the electronegativity of Cu and reducing the bonding energy barrier between Cu and H. This is reflected in the figure as a leftward shift of the peak. The same principle applies to the high-temperature adsorption peak, leading to a leftward shift. Also, the 4% RuP/Cu-500 showed a lower H_2 adsorption capacity than 4% RuP/Cu. This may be one of the reasons why the 4% RuP/Cu catalyst exhibits better hydrogenation activity (see below).

To better demonstrate the LSPR effect of Cu, the basic characterization of the photochemical properties of the catalysts was carried out, as described below (Fig. S3†). As expected, the photocurrent response curves obtained under Xe lamp irradiation (Fig. S3a†) confirmed the significantly lower photocurrent density exhibited by RuP compared to the other two Cu-based catalysts. Compared with the Cu catalyst, 4% RuP/Cu has a relatively low photoresponse current. It is speculated that this is due to the lack of photoactive RuP loading on Cu species. The UV-vis diffuse reflectance spectra (Fig. S3b†) demonstrated that two Cu-based catalysts had an ultrahigh absorbance in the wide
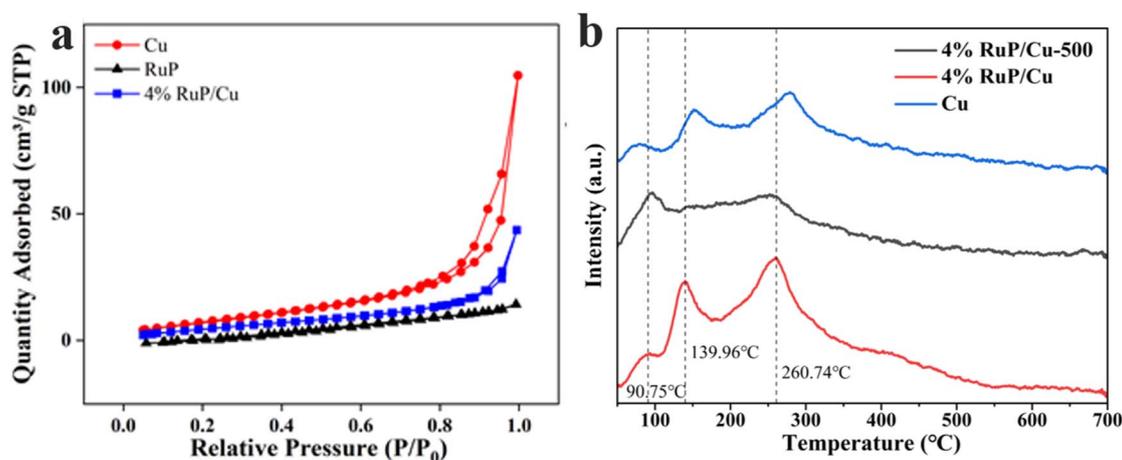

Fig. 3 (a) N_2 adsorption−desorption isotherms of different catalysts; (b) H_2-TPD curves of different catalysts. (4% RuP/Cu-500: calcination of the catalyst precursor at 500 °C in a 10% H_2/Ar atmosphere.)

wavelength range. However, RuP exhibits a different absorption spectrum from conventional photocatalysts. It may be due to its black color rather than the photoactivity. The EIS spectra (Fig. S3c†) demonstrated that the Cu catalyst has the smallest arc radius, indicating the highest electron transfer rate compared to the other two catalysts. The RuP catalyst showed a larger arc radius, suggesting the weak conductivity of amorphous RuP. This also results in a larger arc radius for 4% RuP/Cu catalysts compared to Cu catalysts.

3.2 Catalytic performance evaluation

Initially, the potential products of 4% RuP/Cu in photocatalytic CO_2 hydrogenation were investigated in a self-made fixed-bed reactor, revealing that the products consisted solely of CO and CH_4. The carbon source in the products was tracked by conducting activity tests on x% RuP/Cu under various conditions (Table S2†). The results indicated that CO_2 hydrogenation products triggered by the catalyst or other potential carbon sources were ruled out.

Then, the performance of x% RuP/Cu and reference samples in the photocatalytic CO_2 hydrogenation reaction was assessed (Fig. 4a). The actual loading of x% RuP/Cu catalyst was calculated using ICP-OES (Table S3†). The results show that with the increase in the loading capacity, there is little difference between the actual loading capacity and the theoretical loading capacity of the catalyst. No product formation was detected under the conditions with Cu nanoparticles alone, indicating that Cu was not the active center for the CO_2 hydrogenation

reaction (Fig. 4a). The introduction of RuP led to the production of highly selective CO products by all x% RuP/Cu catalysts, demonstrating that RuP species are the primary active centers and play a catalytic role in the process. The low CO yield from pure RuP suggests that Cu nanoparticles play a significant role in the photocatalytic CO_2 reaction under photothermal conditions. As the RuP content in the catalyst increased, the CO yield exhibited a volcano trend, with the 4% RuP/Cu catalyst reaching a peak under the current conditions. Therefore, subsequent researches were based on 4% RuP/Cu as an object.

To investigate the impact of external thermal conditions on the photocatalytic RWGS reaction, Fig. 4b illustrates the performance of 4% RuP/Cu under dark conditions. Under darkness, the activity of 4% RuP/Cu increased from 1.76 mmol g^{-1} h^{-1} to 19.87 mmol g^{-1} h^{-1} as the temperature was raised from 250 °C to 350 °C. This indicates that sufficient temperature was required to activate CO_2 and facilitate the reaction in the RWGS process. Upon the introduction of light, the yield of CO was further enhanced. At a reaction temperature of 300 °C, the CO yield increased to 123.16 mmol g^{-1} h^{-1} with the addition of light, significantly higher than the yield under dark conditions (17.89 mmol g^{-1} h^{-1}). These results demonstrate that photo-induced hot electrons can markedly enhance their activity under light irradiation. These hot electrons were produced by the LSPR of copper nanoparticles.[30] Those captured from the photothermal energy of Cu nanoparticles can be more effectively transferred to the active center species RuP. The findings indicate that 4% RuP/Cu possesses excellent photocatalytic capabilities under photothermal conditions.
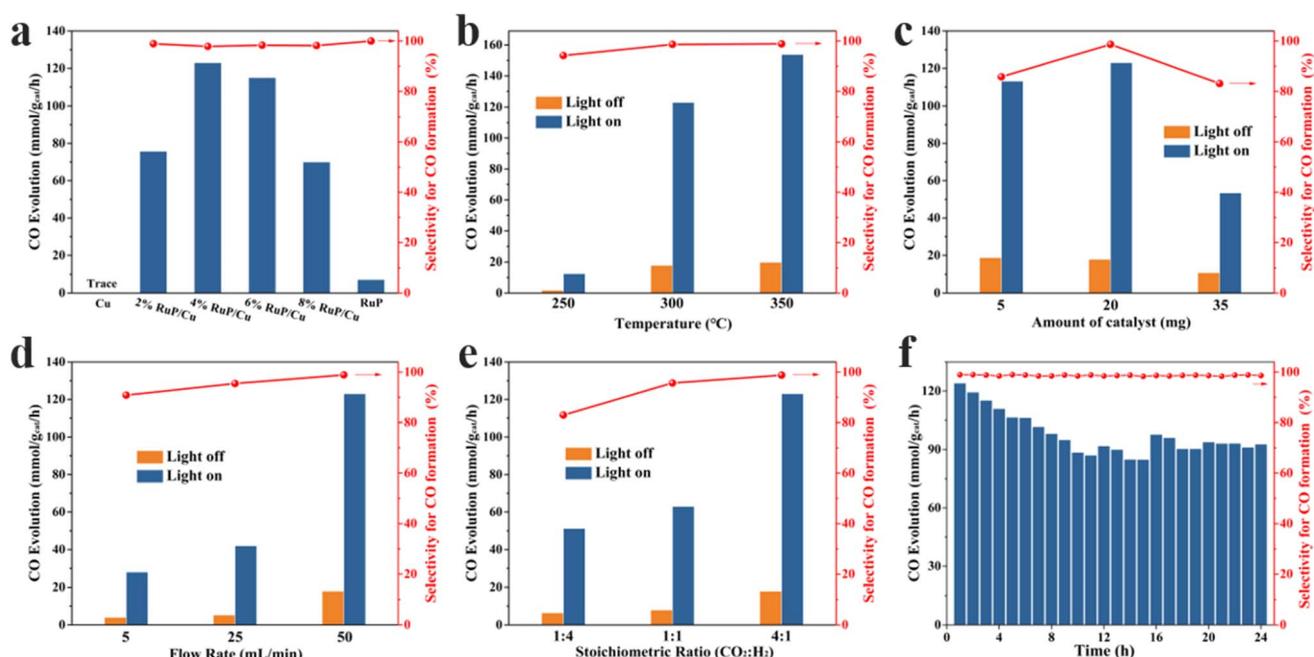

Fig. 4 Performance of the catalysts in CO_2 hydrogenation. (a) Performance of x% RuP/Cu catalysts and reference samples; (b) performance of 4% RuP/Cu at different temperatures, (c) activity of 4% RuP/Cu in different catalyst dosages, (d) activity of 4% RuP/Cu in different feed gas flow rates, (e) activity of 4% RuP/Cu in different CO_2/H_2 ratio of raw gas, and (f) stability of 4% RuP/Cu. (Unless otherwise stated, the reaction condition is fixed: 20 mg catalyst, 300 °C reaction temperature, 500 mW cm^{-2} light intensity, 50 mL min^{-1} flow rate, the stoichiometric ratio of CO_2 : H_2 is 4 : 1, and 1 h reaction period.)

When adjusting the catalyst loading, Fig. 4c indicates that there was no significant difference in the activity between 5 mg and 10 mg of the catalyst, but increasing the catalyst amount to 35 mg resulted in a strong suppression of CO activity. This suggests that an excess of catalyst may inhibit the reaction rate or lead to the incomplete consumption of the reactants. Fig. 4d explores the effect of the feed gas flow rate on the catalytic activity; as the feed gas flow rate increased from 5 mL min^{-1} to 50 mL min^{-1}, the CO yield continuously improved, and the CO selectivity correspondingly increased as well. Fig. 4e displays the reaction activity of the 4% RuP/Cu catalyst under different CO_2/H_2 ratios. Under the same flow conditions, as the proportion of CO_2 increased, the CO yield significantly increased (from 51.21 to 123.16 mmol g^{-1} h^{-1}), and the CO selectivity also continuously improved. This indicates that a higher flow rate or a larger proportion of CO_2 per unit time will reduce its residence on the catalyst, leading to faster desorption of intermediate CO and ultimately enhancing the selectivity of the reaction. Furthermore, there conditions can also increase the production rate of CO.

Traditional copper-based materials often face challenges in widespread application due to the instability of copper; hence, we have examined the stability of the catalyst. As shown in Fig. 4f, during the continuous photocatalytic reaction over 24 hours, the catalyst's initial activity at 121.96 mmol g^{-1} h^{-1} gradually declined with the progression of the reaction, experiencing a decrease of approximately 24.39% and eventually stabilizing at about 92.46 mmol g^{-1} h^{-1}. We attribute the decline in activity to the photothermal effect of the plasmonic metal leading to material sintering as well as the weak interaction between the copper support and the RuP species. Accordingly, we conducted TEM characterization and XPS analysis on the catalyst after 24 hours of reaction, as shown in Fig. S4.† Fig. S4a–c† display the TEM morphology of the catalyst following the stability test, revealing the formation of large RuP particles on the catalyst surface. This aggregation and sintering of the supported RuP is attributed to the photothermal energy generated by the plasmonic effect of Cu. Fig. S4d and e† indicate no change in the bonding mode of P with Ru after the reaction, while the integration of peak areas shows a decrease in P–Ru bonding and an increase in Ru–Ru bonding, further confirming the aggregation of Ru. Plasmonic metals possess the capability to induce strong electromagnetic fields, high-energy charge carriers, and photothermal effects. In the case of Cu, negative values above 400 nm and smaller values above 600 nm result in a strong LSPR response across the entire visible light region and even into the NIR region.[41] This additional energy is ultimately converted into thermal effects, leading to the aggregation and sintering of RuP, thus reducing the number of active sites. In summary, this is identified as the primary cause of the decrease in catalyst activity.

4. Conclusions

In summary, we have proposed a straightforward approach to explore efficient photocatalysts for CO_2 hydrogenation through co-reduction. By leveraging the plasmonic effect of Cu nanoparticles, we demonstrated enhanced CO production rates and high CO selectivity under photocatalytic conditions. Under the optimized conditions, the 4% RuP/Cu catalyst achieved a CO yield of 123.16 mmol g^{-1} h^{-1} with a selectivity of 98.68%. The key to the improved performance lies in the LSPR effect of the plasmonic metal Cu, which effectively harnesses light energy, resulting in an approximately eightfold increase in the activity compared to purely thermal reactions. Additionally, the incorporation of phosphorus leads to the formation of an amorphous phase and modulates the electronic state of Ru, providing abundant active sites for CO_2 adsorption. This work underscores the significance of metal phosphides in maximizing the conversion and selectivity of CO_2 hydrogenation products.

Data availability

Data are available from the authors on request.

Author contributions

Xiuping Li: data curation, formal analysis. Jiaqi Wang: data curation, formal analysis, investigation, writing – original draft. Bolin Yin: data curation. Kaihong Liu: formal analysis, software. Jingjing Zhao: formal analysis, validation. Bo Jiang: data curation, formal analysis writing – review & editing. Hexing Li: conceptualization, funding acquisition, supervision, writing – review & editing.

Conflicts of interest

There are no conflicts to declare.

Acknowledgements

Notes and references

1 D. Voiry, H. S. Shin, K. P. Loh and M. Chhowalla, *Nat. Rev. Chem.*, 2018, **2**, 0105.

2 X. Li, J. Lin, L. Li, Y. Huang, X. Pan, S. E. Collins, Y. Ren, Y. Su, L. Kang, X. Liu, Y. Zhou, H. Wang, A. Wang, B. Qiao, X. Wang and T. Zhang, *Angew. Chem., Int. Ed.*, 2020, **59**, 19983–19989.

3 J. Hu, Y. Cai, J. Xie, D. Hou, L. Yu and D. Deng, *Chem*, 2024, **10**, 1084–1117.

4 A. García-Trenco, A. Regoutz, E. R. White, D. J. Payne, M. S. P. Shaffer and C. K. Williams, *Appl. Catal., B*, 2018, **220**, 9–18.

5 Y. Jiang, Y. Sung, C. Choi, G. Joo Bang, S. Hong, X. Tan, T.-S. Wu, Y.-L. Soo, P. Xiong, M. Meng-Jung Li, L. Hao, Y. Jung and Z. Sun, *Angew. Chem., Int. Ed.*, 2022, **61**, e202203836.

6 T. P. Araújo, S. Mitchell and J. Pérez-Ramírez, *Adv. Mater.*, 2024, 2409322.

7 R. Ramírez-Grau, M. Cabrero-Antonino, H. García and A. Primo, *Appl. Catal., B*, 2024, **341**, 123316.

8 Y. Wang, J. Yang, Y. Sun, D. Ye, B. Shan, S. C. E. Tsang and X. Tu, *Chem*, 2024, **10**, 2590–2606.

9 K. Wang, Y. Zhu, M. Gu, Z. Hu, Y.-C. Chang, C.-W. Pao, Y. Xu and X. Huang, *Adv. Funct. Mater.*, 2023, **33**, 2215148.

10 A. Fedorov, H. Lund, V. A. Kondratenko, E. V. Kondratenko and D. Linke, *Appl. Catal., B*, 2023, **328**, 122505.

11 H. Zhao, R. Yu, S. Ma, K. Xu, Y. Chen, K. Jiang, Y. Fang, C. Zhu, X. Liu, Y. Tang, L. Wu, Y. Wu, Q. Jiang, P. He, Z. Liu and L. Tan, *Nat. Catal.*, 2022, **5**, 818–831.

12 J. Wang, S. Li, J. Zhao, K. Liu, B. Jiang and H. Li, *Appl. Catal., B*, 2024, **352**, 124045.

13 Z. Li, X. Zhang, J. Liu, R. Shi, G. I. N. Waterhouse, X.-D. Wen and T. Zhang, *Adv. Mater.*, 2021, **33**, 2103248.

14 R. Liu, D. Leshchev, E. Stavitski, M. Juneau, J. N. Agwara and M. D. Porosoff, *Appl. Catal., B*, 2021, **284**, 119787.

15 Y. Wang, Y. Zhao, J. Liu, Z. Li, G. I. N. Waterhouse, R. Shi, X. Wen and T. Zhang, *Adv. Energy Mater.*, 2020, **10**, 1902860.

16 Q. Hao, Z. Li, Y. Zhu, Y. Shi, M. Huo, H. Yuan, S. Ouyang and T. Zhang, *Adv. Funct. Mater.*, 2024, 2403848.

17 A. I. M. Rabee, S. Cisneros, D. Zhao, C. R. Kreyenschulte, S. Bartling, V. Kondratenko, C. Kubis, E. V. Kondratenko, A. Brückner and J. Rabeah, *Appl. Catal., B*, 2024, **345**, 123685.

18 R. Zhang, X. Wang, K. Wang, H. Wang, L. Liu, X. Wu, B. Geng, X. Chu, S. Song and H. Zhang, *Adv. Energy Mater.*, 2023, **13**, 2203806.

19 B. Shao, G. Hu, K. A. M. Alkebsi, G. Ye, X. Lin, W. Du, J. Hu, M. Wang, H. Liu and F. Qian, *Energy Environ. Sci.*, 2021, **14**, 2291–2301.

20 F. Sun, X. Xing and H. Hong, *Small*, 2023, **19**, 2203647.

21 A. Wang, C. Bozal-Ginesta, S. G. Hari Kumar, A. Aspuru-Guzik and G. A. Ozin, *Matter*, 2023, **6**, 1334–1347.

22 Y. F. Zhu, B. Xie, R. Amal, E. C. Lovell and J. Scott, *Small Struct.*, 2023, **4**, 2200285.

23 J. Yang, J. Wang, J. Zhao, Y. Bai, H. Du, Q. Wang, B. Jiang and H. Li, *J. CO_2 Util.*, 2022, **57**, 101893.

24 X. Shen, C. Li, Z. Wu, R. Tang, J. Shen, M. Chu, A.-B. Xu, B. Zhang, L. He and X. Zhang, *Nanoscale*, 2022, **14**, 11568–11574.

25 L. Wang, Y. Dong, T. Yan, Z. Hu, F. M. Ali, D. M. Meira, P. N. Duchesne, J. Y. Y. Loh, C. Qiu, E. E. Storey, Y. Xu, W. Sun, M. Ghoussoub, N. P. Kherani, A. S. Helmy and G. A. Ozin, *Nat. Commun.*, 2020, **11**, 2432.

26 L. Zhou, J. M. P. Martirez, J. Finzel, C. Zhang, D. F. Swearer, S. Tian, H. Robatjazi, M. Lou, L. Dong, L. Henderson, P. Christopher, E. A. Carter, P. Nordlander and N. J. Halas, *Nat. Energy*, 2020, **5**, 61–70.

27 S. Zhu, S. Xu, Y. Guo, H. Zhang, K. Ma, J. Wang, Q. Zhao, L. Zhou and W. Cai, *ACS Nano*, 2023, **17**, 10300–10312.

28 H. Jiang, Z. Xing, T. Zhao, Z. Yang, K. Wang, Z. Li, S. Yang, L. Xie and W. Zhou, *Appl. Catal., B*, 2020, **274**, 118947.

29 H. Robatjazi, H. Zhao, D. F. Swearer, N. J. Hogan, L. Zhou, A. Alabastri, M. J. McClain, P. Nordlander and N. J. Halas, *Nat. Commun.*, 2017, **8**, 27.

30 C. Song, Z. Wang, Z. Yin, D. Xiao and D. Ma, *Chem Catal.*, 2022, **2**, 52–83.

31 F. Fresno, A. Iglesias-Juez and J. M. Coronado, *Top. Curr. Chem.*, 2023, **381**, 21.

32 M. Ghoussoub, M. Xia, P. N. Duchesne, D. Segal and G. Ozin, *Energy Environ. Sci.*, 2019, **12**, 1122–1142.

33 J. Yu, Y. Guo, S. She, S. Miao, M. Ni, W. Zhou, M. Liu and Z. Shao, *Adv. Mater.*, 2018, **30**, 1800047.

34 Q. Qin, H. Jang, L. Chen, G. Nam, X. Liu and J. Cho, *Adv. Energy Mater.*, 2018, **8**, 1801478.

35 H. Liao, Y. Sun, C. Dai, Y. Du, S. Xi, F. Liu, L. Yu, Z. Yang, Y. Hou, A. C. Fisher, S. Li and Z. J. Xu, *Nano Energy*, 2018, **50**, 273–280.

36 C. Wu, J. Shen, X. An, Z. Wu, S. Qian, S. Zhang, Z. Wang, B. Song, Y. Cheng, B. Yan, T.-K. Sham, X. Zhang, C. Li, K. Feng and L. He, *ACS Catal.*, 2024, **14**, 8592–8601.

37 S. Jensen, R. Cheula, M. Hedevang, M. Andersen and J. V. Lauritsen, *Angew. Chem., Int. Ed.*, 2024, **63**, e202405554.

38 Y.-I. Kim, K.-B. Kim and M. Kim, *J. Mater. Sci. Technol.*, 2020, **51**, 193–201.

39 W. Li, Y. Zhao, Y. Liu, M. Sun, G. I. N. Waterhouse, B. Huang, K. Zhang, T. Zhang and S. Lu, *Angew. Chem., Int. Ed.*, 2021, **60**, 3290–3298.

40 J. Zhao, J. Wang, Y. Bai, H. Du, J. Yang, B. Yin, B. Jiang and H. Li, *J. CO_2 Util.*, 2023, **74**, 102528.

41 S. W. L. Ng, K. J. H. Lim, M. Gao, W. Lu, T. Ghosh, M. Zhang, S. Kawi, M. Hong and G. W. Ho, *Appl. Catal., B*, 2024, **340**, 123182.